Editors' Suggestion

Velocity and size quantification of drops in single and collective bursting bubbles experiments

B. Néel
Department of Mechanical and Aerospace Engineering, Princeton University, Princeton, New Jersey 08544, USA

L. Deike*
Department of Mechanical and Aerospace Engineering and High Meadows Environmental Institute, Princeton University, Princeton, New Jersey 08544, USA

(Received 12 April 2022; accepted 26 August 2022; published 5 October 2022)

Mechanisms of droplet production from bursting bubbles have been extensively studied for single bubbles, but remain sparsely investigated in more complex collective settings. We discuss jet and film drop velocity-size relationships from physics-based mechanisms as a potential means to further differentiate between various mechanisms and correctly determine the drops origin. We report dynamical experiments of drop production by bursting bubbles in single and collective setups. In the collective bubbling experiment, subsurface quasimonodisperse bubbles are rising up to the surface where, depending on the surfactant concentration, they can either merge or assemble in rafts of monodisperse bubbles. Drop trajectories are recorded, analyzed, and shown to exhibit uniquely distinctive features for the different production mechanisms: centrifuge film drops are ejected sideways, and jet drops are ejected vertically. Different single-burst scalings are finally compared to the experimental size-velocity relationships, and reveal that drops coming from collective bubble bursting appear slower and more scattered than when coming from single bursting bubbles.

DOI: 10.1103/PhysRevFluids.7.103603

I. INTRODUCTION

Drops from bursting bubbles have long been associated with the production of sea spray aerosols: saltwater droplets and salt particles that can remain suspended in the atmosphere [1,2]. Evidence of their existence has been gathered over decades, with direct observations (such as the visible growth of a fog in a supersaturated chamber [3–5]; see Fig. 1 below) as well as indirect measurements of the dried aerosols [6–8].

Since the pioneering works by Woodcock *et al.* [1] and Day [4], large theoretical, numerical, and experimental progress has been made to understand the mechanisms at the core of a single bubble bursting, namely, the jet and film drop mechanisms (see Refs. [9,10]). Extensive work has focused on the associated size, velocity, and number of drops, recently reviewed by Deike [11] and discussed in details in Sec. II. The production of aerosols has been measured in more complex bubbling setups, with bubbles produced in large numbers by blowing air through a porous glass frit [12,13], capillary needles [7,14,15], or venturi devices [16], by electrolysis [8], and by entraining air underwater by means of a plunging jet or waterfall [17–19]. At the ocean surface, bubbles are produced in large quantities by breaking waves [10,11,20], and many attempts have

*ldeike@princeton.edu

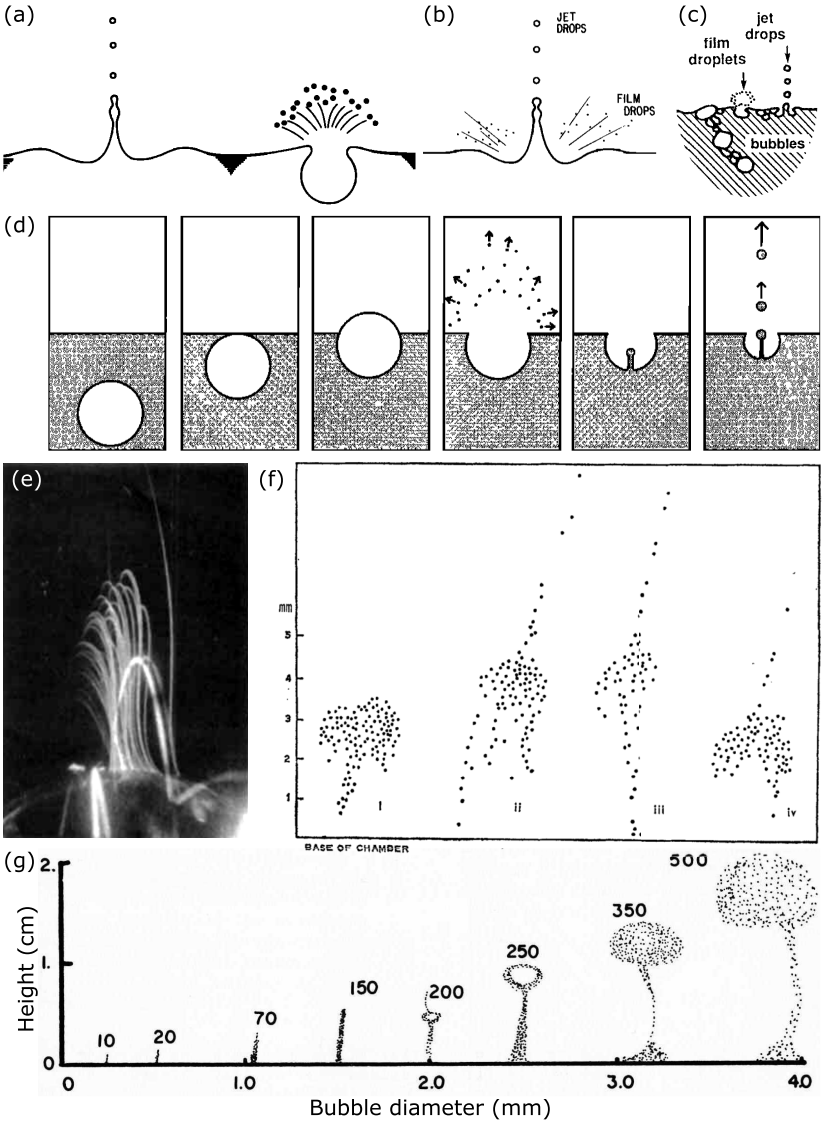

FIG. 1. Historical representations of film drops. (a) Experiments on (jet and) film drops from single bursting bubbles, observed with holography [25]. (b) Experiments on film drops from a train of bubbles (1–3 s^{-1}), measured with an aerosol counter [26]. (c) Review on sea spray production [27]. (d) Monograph on sea spray production [9]. (e) A single bubble bursting (1.1 mm diameter) in a supersaturated cloud chamber [4]. (f) Four single bubbles bursting (1.8 mm diameter) in a cloud chamber [31]. (g) Single bubbles bursting in a cloud chamber [30]. Reproduced with permission from John Wiley and Sons, Springer Nature, and the Canadian Meteorological and Oceanographic Society.

been made to reproduce laboratory bubble distributions mimicking the ones near the sea surface [18,20–22]. In the context of sea spray formation, bubbles produced by nucleation in supersaturated water [23] are not considered, but can be important in other configurations, such as methane emissions [24].

Interpretations of complex bubbling experiments relying on single bursting mechanisms remain incomplete. As shown in Fig. 1, historical representations of the different film and jet drop produc-

tion mechanisms, whether from original research (Figs. 1(a) and 1(b) [25,26]) or review articles (Figs. 1(c) and 1(d) [9,10,27]), do not necessarily depict a unified picture. Even though active and recent research has delivered a very clear understanding of jet drops (down to 0.5 μm for 10 μm bubbles in water [28]) and centrifuge film drops (down to 0.5 μm [29]), the origin of smaller drops (100 nm) remains to be clarified, in particular in more complex bubbling settings. We also note that direct experimental evidence of submicron drops has been reported in supersaturated chambers [4,30,31], as reproduced in Figs. 1(e)–1(g), and remain to be compared with recent measurements of the dry aerosols [7,32]. More precise attributions of the different mechanisms will eventually improve the relative quantification of drops, in size and number, which will benefit the understanding of the droplets' composition, with potential impacts on modeling of atmospheric processes such as radiative balance and cloud formation, in particular in remote marine environments.

This article presents experiments with a controlled production of bubbles in single and collective settings, and the drops they eject when they burst. In complement to the drop size and number, previously reported [15], we present data on their trajectory. We show that this additional piece of knowledge can be used as a confounding factor in mechanism attribution. We first review and discuss different scalings for bursting bubble drops in Sec. II, with a focus on the size-velocity relationships. Then we present a single bursting experiment producing film drops in Sec. III, and describe the size and velocity relationship, together with the angle of ejection. Finally drop dynamics from bubbles bursting in a controlled, collective experiment are shown in Sec. IV, with again an emphasis in the size-velocity relationships, and discussion on the mechanism at the origin of the drops.

II. SCALINGS FOR BURSTING BUBBLE DROPS SIZE AND VELOCITY

A. Jet drops

Jet drops are produced as the jet formed during the collapse of the bubble cavity destabilizes according to the Plateau-Rayleigh mechanism. The jet having a mostly vertical upward trajectory, it follows that jet drops travel along mostly vertical upward trajectories, as observed as early as Ref. [1]. In the same time as it destabilizes, the jet is also pulled down by capillary action, and drops formed later will have a slower ejection velocity [33]. However, most attempts at modeling the drop ejection have focused on the vertical velocity w (coinciding with the total velocity v) and radius r of the first drop. For a bubble with radius R in the ranges $R/\ell_c < 1$ and $900 < R/\ell_\mu < 10^5$, we consider the scalings by Deike *et al.* [33,34], which add gravity to the initial scalings by Gañán-Calvo [35]. Eliminating the bubble radius R, they can be written as

$$\frac{w}{V_\mu} = \alpha_J \left(1 + \delta_J \left(\frac{\ell_\mu}{\ell_c}\right)^2 \left(\frac{r}{\ell_\mu}\right)^{8/5}\right)^{-3/4} \left(\frac{r}{\ell_\mu}\right)^{-3/5}, \tag{1}$$

with $\alpha_J = 13.6$ and $\delta_J = 2680$ fitted on experimental and numerical data [33–35], with an uncertainty estimated at 20%; $\ell_\mu = \mu^2/\gamma\rho$, $\ell_c = \sqrt{\gamma/\rho g}$, and $V_\mu = \gamma/\mu$, with μ the water dynamic viscosity, ρ its density, γ the surface tension and g the gravitational acceleration. Equation (1), which depends on the liquid properties via the Morton number $\mathrm{Mo} = (\ell_\mu/\ell_c)^2$, was validated experimentally and numerically for multiple liquids and a wide range of bubble sizes [33,36,37]. Although other scalings have been derived and adjusted with a better precision on experimental and numerical data [38,39], Eq. (1) relies on a reduced number of adjustable parameters and presents an explicit form for the velocity-size relationship, and is used here for simplicity. For a given liquid (i.e., fixed lengths ℓ_c and ℓ_μ), the asymptotic behavior for bubbles smaller than the capillary length (radius $R \ll \ell_c$) can be written as [35]

$$\frac{w}{V_\mu} = \alpha_J \left(\frac{r}{\ell_\mu}\right)^{-3/5}. \tag{2}$$

Gordillo and coauthors [40,41] developed an alternative scaling based on the capillary wave focusing at the bottom of the cavity, which relates the first drop size and velocity according to

$$\frac{r}{\ell_\mu} = \beta_J \left(\frac{w}{V_\mu}\right)^{-4/3} \left(1 - \gamma_J \left(\frac{w}{V_\mu}\right)^{1/3}\right), \tag{3}$$

with $\beta_J = 365$ and $\gamma_J = 0.88$. Again, the uncertainty on these coefficients is about 20%. Though relying on different derivations, the two scalings, validated against the same experimental data, compare well with each other for bubbles small when compared to ℓ_c, as was shown in Refs. [11,28] (see also Fig. 6 below).

B. Film drops

According to the current and most general understanding, film drops originate from the fragmentation, or shattering, of the bubble cap film at bursting. When compared to jet drops, this naturally leads to different sizes and velocities, as reviewed in Fig. 2 of Ref. [10]. However, the unique denomination encompasses a variety of mechanisms, leading to different subcategories of drops. To the best of our knowledge, three mechanisms have been identified so far: splash drops [42], centrifuge drops [25,29,43], and recently flap drops [32]. The splash drops mechanism was proposed by Spiel [42] as an answer to the submicronic drop production peak observed for bubbles around 1 mm in radius [26,44]. In this model, drops are produced when the undestabilized bubble cap rim impacts against the bubble edge. No later study has been found to confirm or discard this mechanism.

Centrifuge drops are the result of two successive destabilizations. First, the cap film rim destabilizes into ligaments according to a Rayleigh-Taylor instability, driven by the centripetal acceleration associated with the rim retraction along the spherical cap [43]. Then the ligaments break up into droplets via a Plateau-Rayleigh instability [25,29]. We relate the drop ejection velocity $v = \sqrt{u^2 + w^2}$ (with u and w the horizontal and vertical components, respectively) to their radius r by combining the following expressions and eliminating the dependence in the bubble radius R and cap film thickness H. Reference [43] measures the bubble-averaged drop velocity $\langle v \rangle$ as 80% of the rim retraction velocity $V_{TC} = \sqrt{2\gamma/\rho H}$, and Ref. [29] predicts that the drop mean size varies as $\langle r \rangle \propto R^{3/8} H^{5/8}$ with the film thickness at bursting $H \approx R^2/\mathcal{L}$, which for bubble radii $1 < R/\ell_c < 5$ combine into

$$\frac{\langle v \rangle}{V_\mathcal{L}} = \alpha_F \left(\frac{\langle r \rangle}{\mathcal{L}}\right)^{-8/13}, \tag{4}$$

with $\alpha_F = 0.77$, $\mathcal{L} = 20$ m, and $V_\mathcal{L} = \sqrt{2\gamma/\rho\mathcal{L}}$. The length $\mathcal{L}$, identified by Lhuissier and Villermaux [29], is interpreted theoretically by Poulain *et al.* [45] as the result of a competition between the residence time of a contaminant at the interface and its shear-enhanced diffusion time across the film, which leads to the bubble rupture: $\mathcal{L} \propto (\nu/D)^{2/3} \ell_c$ (with D the diffusion coefficient of the contaminant and ν the kinematic viscosity of the film liquid).

The model of flap drops, recently published by Jiang *et al.* [32], considers the role of the surrounding atmosphere in the drop production. The density ratio drives a Squire, or flapping, instability [46], from which tiny drops are expelled. Such small drops (<1 μm) are not measurable by classic optical techniques, and have been identified by relying on measurements of the associated dried aerosols by means of a condensation particle counter, an instrument also used in previous studies on film drops from single bursting bubbles [26,47]. The link between the sizes of the drops at production and the sizes of the dry aerosol particles then requires a model of evaporation: for seawater, the dry aerosol particles are usually considered four times as large as the drops at production [9,10]. The size resolution, as low as 10 nm, allowed the authors to retrieve the aerosol production peak around 100 nm (in terms of dry aerosol diameter) observed in many studies [7,12,19,26,47].

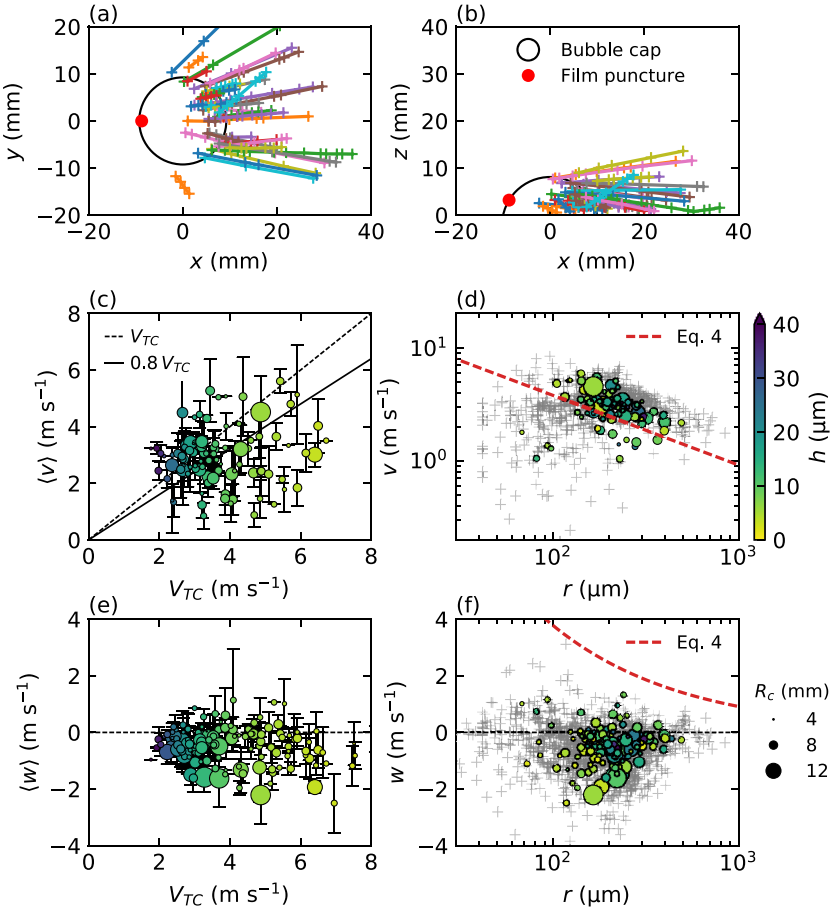

FIG. 2. Film drops from single bursting experiments. (a) Top and (b) side views of a $R_c = 10.2$ mm cap radius bubble bursting (black circle) into droplets (colored trajectories). (c, d) Drop absolute velocity v, for each drop (gray pluses) or averaged per bubble $\langle v \rangle$ (colored circles) compared to (c) the film Taylor-Culick opening velocity $V_{TC} = \sqrt{2\gamma/\rho H}$ and (d) the drop radius r. Circle color and size respectively encode the bubble film thickness and cap radius. (e, f) Same plots for the drop vertical velocity w and bubble average $\langle w \rangle$. The red dashed line is the scaling (4).

III. SIZE AND VELOCITY OF CENTRIFUGE FILM DROPS FROM SINGLE BURSTING

A. Setup

A first experiment is performed to track drops produced by a single bursting bubble, in three dimensions. Filtered, dust-free air is blown through a needle (inner diameter 610 μm) at the bottom of a petri dish (90 mm diameter, 13 mm depth) filled with deionized water at room temperature, to form single bubbles with cap radius R_c ranging from 4 to 15 mm. Once formed, the bubble is let free to evolve at the water surface, and to ultimately burst spontaneously, far from the container edges.

The dynamics of bubble bursting and drop ejection is recorded by means of two high-speed cameras looking respectively sideways and from the top down at the bubble, against uniform white LED backgrounds. Ejected drops are individually tracked and matched on all synchronized frames, to reconstruct to their full tridimensional, time-resolved trajectory at ejection, as illustrated in Figs. 2(a) and 2(b). Their size is measured on the view with the best spatial resolution, down to

23 μm per pixel, after carefully checking that they are in focus. This joint measurement of size and velocity, for each individual drop and to the best of our knowledge, has not been reported before.

The cleanliness of the water and its interface with air led to some deviations with other published results on film drops [29,43]. On the one hand, the film rupture was not systematically observed to occur at the base of the bubble, but rather at different locations up to the top of the bubble, which has a strong impact on the ejection direction of the drops. On the other hand, most bubble cap films were measured to burst at thicknesses larger than the prediction by Lhuissier and Villermaux [29], an *a posteriori* indication of shorter drainage time and bubble lifetime, or greater film instability. As a consequence, we observe a maximum of 44 drops for a 13.3-mm cap radius bubble. For comparison, other experiments observed up to around 110 drops for a 6.3 mm volume-equivalent radius bubble in saltwater [43], 210 drops for a 12 mm cap radius bubble in tap water [29], 255 drops for a 15.9 mm cap radius bubble in saltwater, and 35 drops for a 5.9 mm cap radius bubble in deionized water [48]. (The cap radius is between $2^{1/3} \simeq 1.26$ (bubbles larger than ℓ_c) and 2 (bubbles smaller than ℓ_c) times as large as the volume-equivalent radius [49,50].)

B. Velocity-size relationship

Film drops are ejected in a direction largely determined by the puncture location on the bubble cap. Figures 2(a) and 2(b) show the drop trajectories for a large $R_c = 10.2$ mm bubble. Except for a single drop (an anecdotal splash, as was observed occasionally), all drop trajectories originate and diverge from the location of the initial film puncture. Surface bubbles being at most half spheres emerging from the water, centrifuge film drop trajectories are, according to the mechanism we are presently documenting, constrained to remain at a low angle with respect to the water surface [Fig. 2(b)].

We compare the drop absolute and vertical velocities to the bubble cap film opening velocity, as well as the drop size, in Figs. 2(c)–2(f). In the mechanism proposed in Ref. [29], the film drop production is mediated by the formation and destabilization of ligaments, themselves coming from the destabilization of the retracting cap film rim. The drop formation thus occurs as the rim is traveling, whose velocity gives a first estimate to the drop ejection velocity, if we neglect temporarily the details of the ligament destabilization mechanism. Reference [43] measured the drop velocity to be 80% of the rim retraction velocity $V_{TC} = \sqrt{2\gamma/\rho H}$, also known as the Taylor-Culick velocity, set by the film thickness H. Figure 2(c) shows the drop velocity $\langle v \rangle$ (averaged per bubble) as a function of V_{TC}, and validates this order of magnitude. However, significant scatter around the mean as well as across different bubble sizes and film thicknesses is observed.

Figure 2(e) then shows only the vertical component of the drop velocity $\langle w \rangle$, averaged per bubble, as a function of V_{TC}. It represents only a small fraction of V_{TC} and is largely negative, and even more so as bubbles are bigger. We draw two conclusions: (1) centrifuge film drops are traveling mostly downwards, at a small angle with respect to the water surface with which they collide and merge quickly, and (2) the Taylor-Culick velocity alone (that is the bubble cap film thickness) does not capture the drop vertical ejection velocity correctly, as it mostly represents the horizontal velocity.

Figure 2(d) shows the drop velocity $v = \sqrt{u^2 + w^2}$ as a function of its radius r, for all drops (gray pluses) and for their bubble-averaged values (colored circles). The averaged data tend to agree well with the prediction (4) by Lhuissier and Villermaux [29], despite large scatter both for each bubble and in the average trend. Similarly, Fig. 2(f) shows the drop vertical velocity w as a function of its radius r, for all drops (gray pluses) and for their bubble-averaged values (colored circle). As in Fig. 2(e), points lie under the scaling (4), the vertical component w accounting only for a small fraction of the velocity norm v.

From this experiment on centrifuge film drops from single bursting bubbles, we conclude that the velocity-size relationship derived from Refs. [29,43] captures well the mean behavior of drops, within a somewhat large scatter. A reason for this large scatter may be the use of relatively clean water, when compared to Refs. [29,43], leading to a greater bubble cap instability and thicker films. Some variability in the film puncture location, not always occurring at the foot of the bubble, may

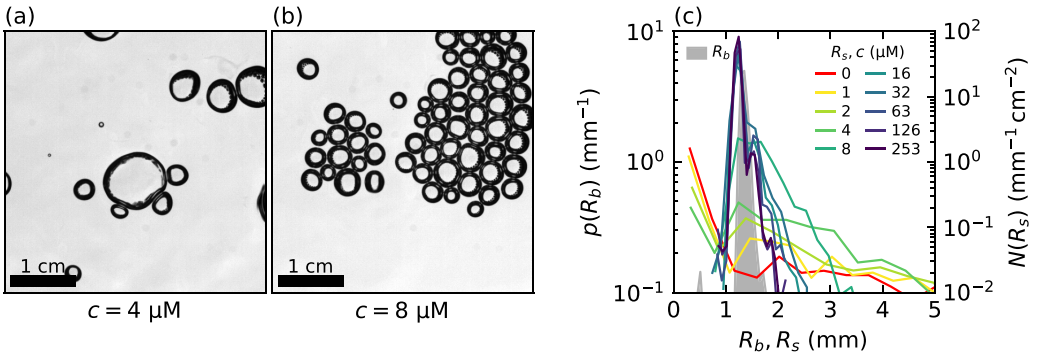

FIG. 3. Experimental setup. (a, b) Representative views of the bubbles at the surface, respectively below and at the coalescence transition (SDS, $c_* = 8\,\mu$M). (a) Below the transition, coalescence and as a consequence large bubbles are commonly observed. (b) Above the transition, coalescence is suppressed and bubbles cluster in almost monodisperse rafts. (c) Subsurface R_b (shaded gray) and surface R_s (colored lines) bubble radius distributions $p(R_b), N(R_s)$, respectively. From a nearly Gaussian distribution of subsurface bubbles, surface bubbles transition from long-tailed distributions (red and yellow lines, $c < c_*$) to nearly Gaussian distributions (blue lines, $c > c_*$).

also add to the large variability. The drop ejection trajectories are shown to lie at a low angle with respect to the water surface, with a slight preference for going downwards, and diverging from the puncture location. These observations will be used to distinguish the production process in the collective bursting experiments, presented in the next section.

IV. COLLECTIVE BURSTING

Single burst experiments on jet and centrifuge film drops provided scalings between drop sizes and ejection velocities, gathered in Sec. II and compared to film drops in Sec. III. We now compare them to drops from bubbles bursting in a collective experiment (presented briefly in Sec. IV A 1, and at length in Refs. [14,15]). Trajectories of drops from *a priori* unknown origin are compared to typical trajectories for jet drops (mostly vertical) and centrifuge film drops (mostly horizontal), and used as a complementary tool to directly discriminate between the two mechanisms. The framework for analyzing the drop trajectory is developed in Sec. IV A 2, before being applied on jet and film drop trajectories in Sec. IV B. Size-velocity relationships for drops from bursting bubbles are finally discussed under various surface collective states in Sec. IV C.

A. Experimental methods

1. Setup

In the collective bursting experiment, millimetric monodisperse air bubbles (mean volume-equivalent radius $\langle R_b \rangle = 1.35 \pm 0.07$ mm) are introduced at a large rate (between 1600 and 2000 s^{-1}) at the surface of a water pool (60 × 60 cm^2). There, they are free to interact, rearrange, coalesce, and ultimately burst, producing droplets. The concentration of surfactant c added in the water (sodium dodecyl sulfate or SDS in this study) is varied from $c = 0$ to $c = 253\ \mu$M as a way to tune collective effects experienced by the surface bubbles, as detailed comprehensively in Ref. [14]. Figure 3 illustrates different surface bubble arrangements, from merging [Fig. 3(a)] to assembling into clusters [Fig. 3(b)]. Figure 3(c) shows the subsurface R_b and surface R_s bubble radius distributions for different concentrations. For the same subsurface bubble size distribution $p(R_b)$ (shaded gray line), the surface bubble radius distributions $N_s(R_s)$ get narrower around $\langle R_b \rangle$, with larger amplitudes as the surfactant concentration c increases (colored lines).

We described the production of droplets from such collectively bursting bubbles from a statistical point of view in Ref. [15]. We showed in Ref. [14] that the surfactant concentration has a strong influence on the surface bubble arrangements, and as a consequence on the droplet numbers and sizes, for radii $r > 35$ μm. More precisely, the droplet production is optimal around a transition coalescence c_*, identified for subsurface bubbles in Refs. [51,52]. Below $c < c_*$, bubbles can coalesce and the resulting broad surface size distribution leads to broad, multimodal drop size distributions, indicating that multiple bursting mechanisms may be at play. Around and above $c \geqslant c_*$, bubbles do not coalesce and burst in an efficient way, while forming small rafts or being isolated. The assumption of a jet drop mechanism from monodisperse single surface bubbles has been proposed to explain the drop size distribution [15]. At higher surfactant concentrations, surface bubble lifetimes are increasingly longer and bubbles assemble in rafts and foams covering the whole surface, inhibiting the drop production.

In the present article, we focus on the drop dynamics and vertical trajectories. Drops are recorded from the side, on a field of view of vertical extent of 75 mm located a few millimeters above the water surface, by means of a telecentric lens attached to a high-resolution fast camera (frame rate 1 kHz, spatial resolution 36.3 μm per pixel). Drops are detected automatically by way of image processing, and tracked along time. We analyze the drop trajectories $\{x(t), z(t)\}$ within the framework presented in the following section. On a few occasions, the analysis is taken one step further and we manually trace the origin of several drops to single bubble bursting events, even though they are located below the field of view.

2. Drop vertical trajectory: Theoretical considerations

When produced by a bursting bubble, drops are given an initial velocity $\mathbf{v}_0$ and radius r, both functions of the production mechanism. Once they are formed, they are evolving in the air and must verify jointly mass and momentum conservations [10]. In the present experiment, drops are detected down to 110 μm (6 pixels in diameter) and their radius is not observed to vary in the course of their trajectory, with the latter lasting between 80 and 400 ms. Mass is thus conserved and we safely neglect evaporation (see Ref. [36] for considerations on the evaporation of jet drops). In quiescent air, we omit all terms other than drop weight $m\mathbf{g}$ and drag force $\mathbf{F}_D$, to write the drop equation of momentum:

$$m\dot{\mathbf{v}}(t) = \mathbf{F}_D + m\mathbf{g}, \tag{5}$$

with $\mathbf{v}$ the drop velocity, $m = 4\pi\rho r^3/3$ its mass, and ρ the liquid density. Precise expressions for the drag coefficient $C_D = 24C_f/\mathrm{Re}$ in the drag force have been derived elsewhere [10,36,53,54], as a function of the drop Reynolds number $\mathrm{Re} = 2rw_0/\nu_a$, with $\nu_a = \eta_a/\rho_a$ the air kinematic viscosity, η_a its dynamic viscosity, ρ_a its density, and C_f an empirical correction factor. Equation (5) is made nondimensional with w_0 the drop initial vertical velocity and w_0/g the gravity fallout time (nondimensional coordinates are denoted with tildes), and projected on the upwards vertical component w:

$$\tilde{w}'(\tilde{t}) = \frac{w(tg/w_0)}{w_0} = -\frac{C_f}{\mathrm{St}}\tilde{w}(\tilde{t}) - 1, \quad \text{with } \mathrm{St} = \frac{2\rho g r^2}{9\eta_a w_0}. \tag{6}$$

The Stokes number St directly compares the drop inertial response time $\tau = 2\rho r^2/9\eta_a$ to the gravity fallout time w_0/g. We start by simplifying one step further to consider a purely viscous drag $C_D = 24/\mathrm{Re}$ (i.e., $C_f = 1$), in order to solve analytically the drop vertical momentum equation. A double integration of Eq. (6) with $w(t = 0) = V$ and $z(t = 0) = 0$ gives the vertical drop coordinate $z(t)$:

$$\tilde{z}(\tilde{t}) = \mathrm{St}[(1 + \mathrm{St})\left(1 - e^{-\tilde{t}/\mathrm{St}}\right) - \tilde{t}]. \tag{7}$$

Figure 4(a) shows trajectories $z(t)$ for different Stokes numbers, and illustrates the transition from viscosity-dampened trajectories [$\mathrm{St} \ll 1$ or small, fast drops according to Eq. (6)] to parabolic trajectories ($\mathrm{St} \gg 1$ or large, slow drops) as St is increased. The expressions for $z_{\max}$, the maximal

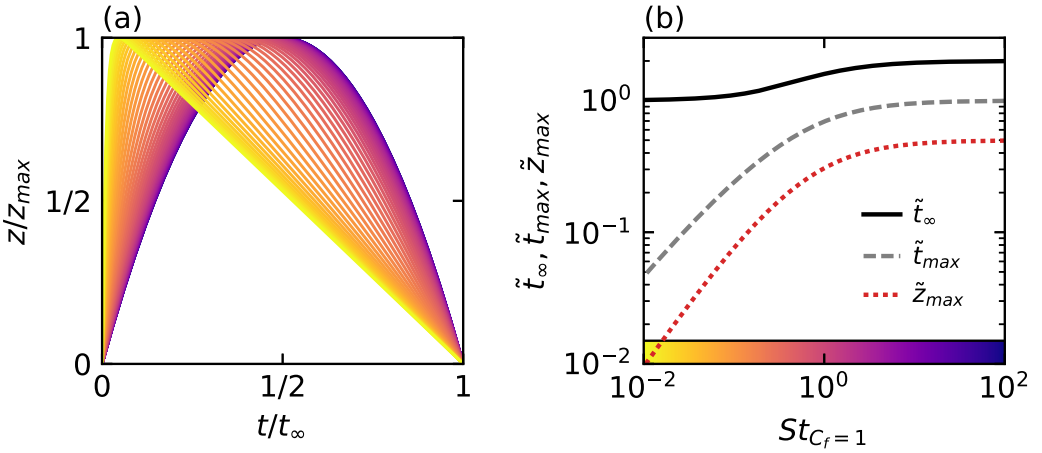

FIG. 4. (a) Trajectories $z(t)$ for different Stokes numbers, with $C_f = 1$ [Eq. (7)], scaled by the fallout time t_∞ and maximal height $z_{\max}$. Color bar is drawn in (b). (b) Nondimensional fallout time $\tilde{t}_\infty = t_\infty g/w_0$ and maximal drop height $\tilde{z}_{\max} = z_{\max} g/w_0^2$ as a function of St.

altitude reached by the droplet, and t_∞ its fallout time, used to scale the trajectories in Fig. 4(a), are plotted with respect to the Stokes number in Fig. 4(b) and given in the Appendix. The measure of St [Eq. (6)], or equivalently of the drop trajectory shape, provides an independent, aerodynamic measurement of the drop radius r:

$$r = 3\sqrt{\frac{\eta_a w_0}{2\rho g}}\mathrm{St}, \tag{8}$$

which we will use in the following paragraphs, either taking $C_f = 1$ (in Fig. 5) or an expression better suited to higher Reynolds number (in Fig. 6 and the Appendix).

B. Jet vs film drop trajectories

Figure 5 shows typical drop trajectories from two bubble bursting events, singled out from the constant stream of bubbles popping at the water surface [Figs. 5(a) and 5(b), in the x-z plane, and Figs. 5(c) and 5(d), as the vertical coordinate $z(t)$]. Even though the bubble bursts below the field of view and some high-reaching drops exit it from above before falling back into the frame, the drop trajectories exhibit distinctive signatures that allow for a reliable mechanism attribution, whether film or jet drops. On the left column [Figs. 5(a) and 5(c)], 14 drops are observed coming from the left in a rather dispersed order, at a low angle with respect to the water surface [Fig. 5(a)]. They do not reach high distances above the surface, and fall back off quickly, after having covered a long horizontal distance. In this case, the water is contaminated by surfactants below the coalescence transition ($c = 4 < c_* = 8\,\mu$M, with SDS). As a consequence, large bubbles can form by successive merging events, as supported by Figs. 3(a) and 3(c), which are more prone to burst into film drops (see Sec. III). Altogether, the sideways drop trajectories and the existence of surface bubbles larger than $R_s \gtrsim \ell_c$ (a loose lower bound for film drops [11,29]) argue for a centrifuge film drop mechanism.

On the right column [Figs. 5(b) and 5(d)], seven drops appear in a vertical train, shooting upwards with little horizontal dispersion, before falling off at a short distance from where they initially emerged [Fig. 5(b)]. The smallest ones (with aerodynamic radius $r = 60\,\mu$m) can reach a vertical height of $z_{\max} = 11$ cm, against $z_{\max} = 3$ cm and less for the largest ones [$r = 120\,\mu$m, Fig. 5(d)]. In this case, the surfactant concentration is equal to the coalescence transition $c = c_* = 8\,\mu$M and surface bubbles barely merge: their distribution is a narrow Gaussian centered on the subsurface

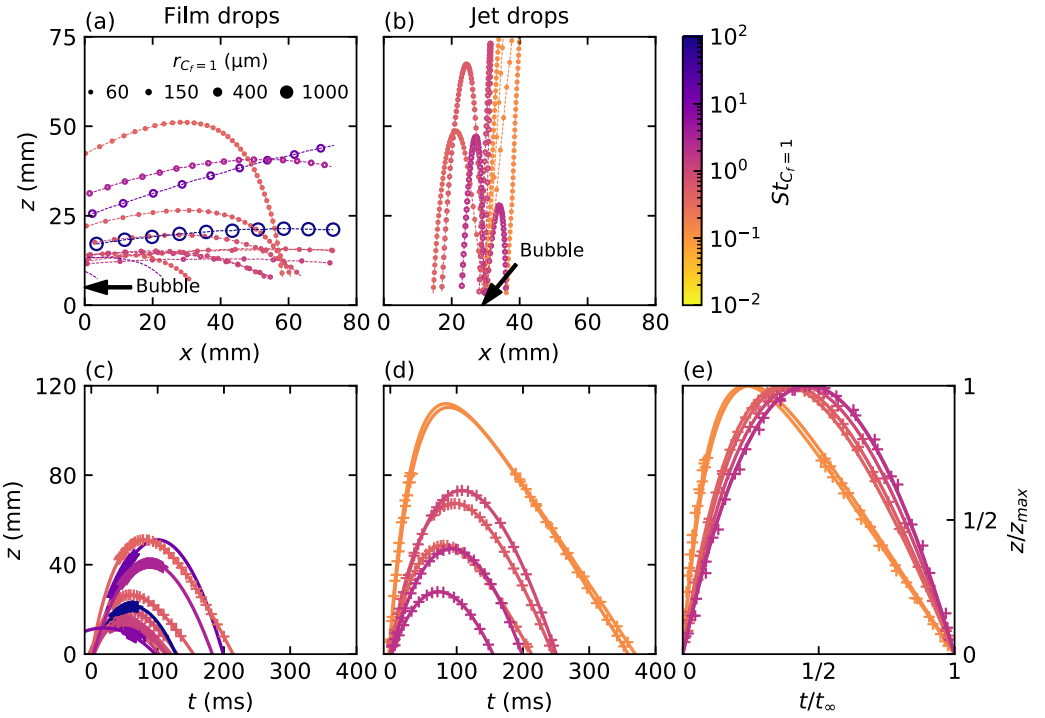

FIG. 5. Typical trajectories for centrifuge film drops [left column or (a, c), in deionized water with SDS, $c = 4$ μM] and jet drops [center and right columns or (b, d, e), $c = 8$ μM]. (a, b) Drop trajectories as observed in the x-z plane, colored by their Stokes number. The circle size indicates the drop radius, and is shown every 4 ms. (c, d) Vertical coordinate z as a function of time t, measured (pluses) and fitted by Eq. (7) (lines). (e) Jet drop vertical trajectories [from (d)], rescaled by their fitted fallout time t_∞ and maximal altitude $z_{\max}$.

size $\langle R_b \rangle = 1.35$ mm [see Figs. 3(b) and 3(c)]. Surface bubbles this size are known to produce around three jet drops in uncontaminated waters [33,36,55]. Altogether, the vertical trajectories and the surface bubble size argue for a jet drop mechanism. The number of drops per bubble is relatively larger than existing predictions [33] and could be attributed to either a collective effect or a modification of the jetting process by the small surfactant contamination.

In Figs. 5(c) and 5(d), we plot the drop vertical coordinate z as a function of time t. The simplified Eq. (7) with $C_f = 1$ (solid line) is adjusted on experimental data (pluses) with a good agreement, to immediately provide an estimate for the Stokes number $\mathrm{St}_{C_f=1}$ (colors) and aerodynamic radius $r_{C_f=1}$ [marker size in Figs. 5(a) and 5(b)], but also the fallout time t_∞ and maximal altitude $z_{\max}$, which are not always readily available from the measurement. For jet drops, we plot the nondimensional jet drop trajectories [from Fig. 5(d)] on Fig. 5(e), which compares successfully with Fig. 4(a). Altogether, the different spatial $\{x, z\}$ and vertical $z(t)$ trajectories for jet and centrifuge film drops allow for a clear distinction: jet drops are shot upwards, whereas centrifuge film drops are ejected sideways and reach lower altitudes. Even though centrifuge film drops travel longer horizontal distances, jet drops spend longer time in quiescent air.

C. Velocity-radius relationships

Figure 6 shows the drop vertical ejection velocity w_0 as a function of its aerodynamic radius r, for drops from bubbles bursting at the surface of water under different concentrations of surfactant SDS. Both quantities are extracted from the numerical fit of Eq. (7) on experimental drop trajectories,

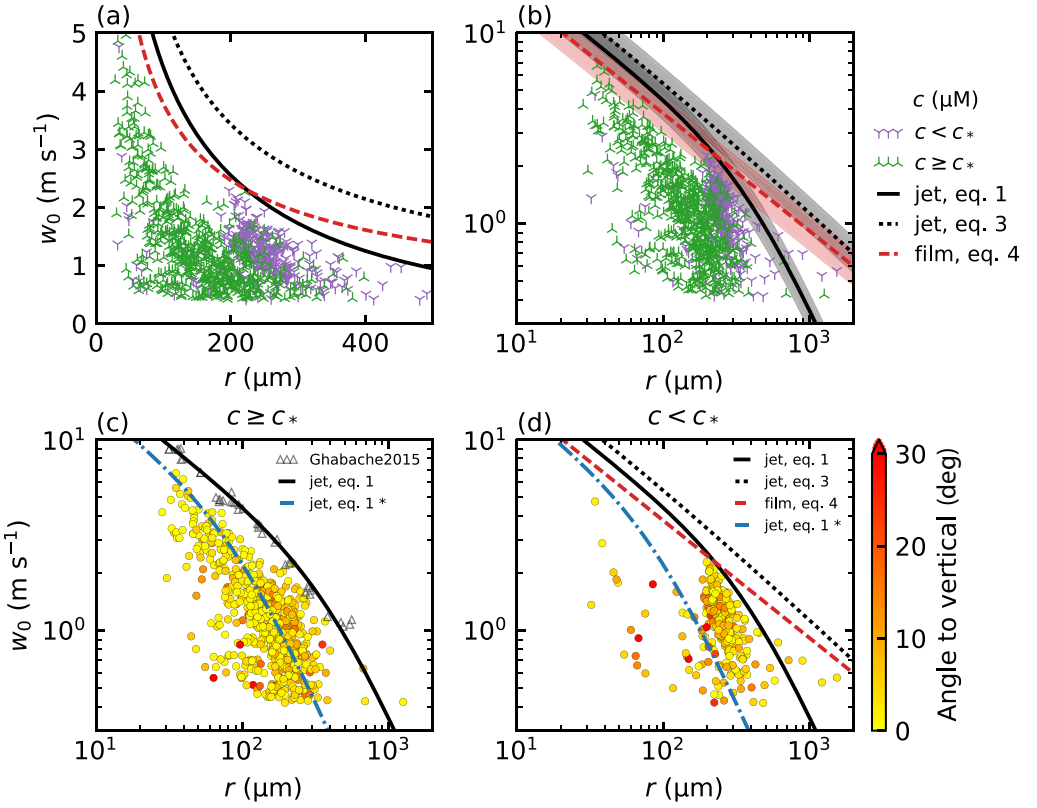

FIG. 6. Drop vertical ejection velocity $w_0 = \dot{z}(t = 0)$ as a function of its radius $r = 3\sqrt{\eta_a w_0 \mathrm{St}/2\rho g}$ in (a) linear and (b–d) logarithmic scales. Equation (7) is fitted on experimental trajectories using the drag correction factor C_f [Eq. (A2)] [56]. Lines are scalings (1–4), with a ±20% deviation plotted on (b). (a, b) Drops are colored according to the water surfactant concentration, below $c < c_*$ (purple symbols) and above $c \geqslant c_*$ (green symbols), the coalescence transition ($c_* = 8\ \mu$M). (c) Drops for $c \geqslant c_*$ are colored according to their ejection angle to vertical $\theta = \arctan(\bar{u}/w_0)$ ($\theta = 0$ for a vertical ejection). Our data are compared with jet drops from single bursting bubbles in water from Ref. [57] (black triangles) and the scaling (1) with newly adjusted parameters (dashed blue line). (d) Drops for $c < c_*$, compared with the scalings (1–4).

using the drag correction factor C_f [Eq. (A2)] by Clift and Gauvin [56]. The experimental points represent indistinctly jet and film drops and are compared to their respective scalings (1) (solid black line), (3) (dotted black line) and (4) (dashed red line), with no *a priori* knowledge of the bursting bubble. We first remark that despite the different mechanisms involved, all jet and film drop scalings exhibit similar power-law trends for radii $r < 200\ \mu$m, and range in comparable orders of magnitude. This can be related to the fact that in all mechanisms the force driving the drop ejection is surface tension, or capillarity. For jet drops bigger than $r > 200\ \mu$m, only the scaling (1) incorporates the effect of gravity on bubbles above the capillary size ℓ_c. As a consequence, it predicts a velocity w_0 decreasing faster with the drop radius r, in agreement with the trend outlined by the drops in the collective bursting experiment, even though the scaling overestimates the experimental data.

The coalescence transition c_*, a feature of the bubble behavior at the surface, also separates the drops into two distinct categories. Figures 6(a) and 6(b) show the velocity-size relationship in linear and logarithmic scales, respectively, with the experimental points sorted with respect to their surfactant concentration: above the transition ($c \geqslant c_*$, green markers) and below ($c < c_*$, purple markers). The same data are plotted separately in Fig. 6(c) ($c \geqslant c_*$) and Fig. 6(d) ($c < c_*$), with

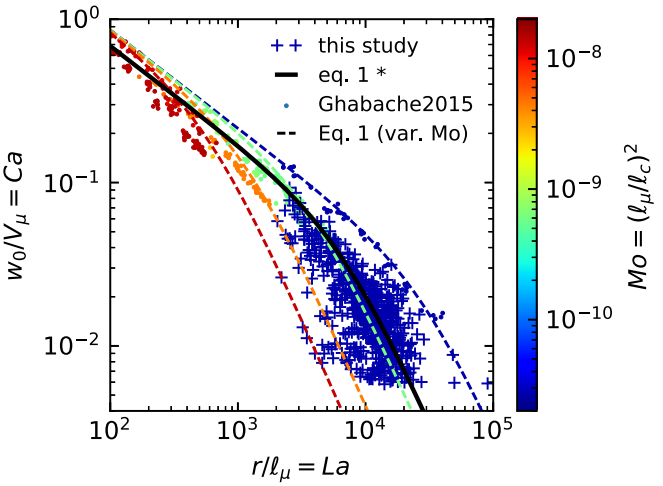

FIG. 7. Nondimensional drop ejection velocity $w_0/V_\mu (= \mathrm{Ca})$ as a function of its radius $r/\ell_\mu (= \mathrm{La})$, for $c \geqslant c_*$. Our data from collective bursting (pluses) are compared to single-bursting experiments in different liquids in Ref. [57] (dots, colored by the liquid Morton number $\mathrm{Mo} = (\ell_\mu/\ell_c)^2$) and the corresponding scaling (1) with original parameters $\alpha_J = 13.6$, $\delta_J = 2680$ (thin dashed colored lines, variable Mo). In the collective experiment, a drop of a given size is ejected at a slower velocity than in a single bursting (blue pluses vs dots), a trend which is better captured by a modified set of parameters in the scaling 1: $\alpha_J = 10.9$, $\delta_J = 26.8 \times 10^3$ (thick solid black line).

the symbol color indicating the ejection angle to vertical, $\theta = \arctan \bar{u}/w_0$ ($\bar{u}$ is the drop horizontal velocity, averaged on the first few points of its trajectory; note that it is always a projection within the depth of field of the optical setup, around 2 cm, and therefore may slightly underestimate the actual horizontal velocity value).

Above the coalescence transition $c \geqslant c_*$, surface bubbles do not merge, and their radius is normally distributed around a mean $\langle R_s \rangle = 1.35$ mm [similarly to the subsurface bubble distribution; see Figs. 3(b) and 3(c)]. Single bubbles this size are known to produce jet drops [33], which Fig. 6(c) and, later, Fig. 7 confirm unambiguously. On the one hand, the vast majority of the drops have ejection angles below $\theta < 10^\circ$; i.e., they exhibit almost exclusively vertical trajectories, a distinctive feature of jet drops. On the other hand, the drop vertical velocity w_0 decreases with an increasing radius r and follows well the trend (1), even though the latter overestimates our data. We plot for reference experimental data obtained for single bubble bursting producing jet drops [57] [Fig. 6, black triangles, on which the scaling (1) is originally fitted], which lies above our data. A new estimate of the adjustable parameters $\alpha_J = 10.9$ and $\delta_J = 26.8 \times 10^3$ in the scaling (1) is proposed and captures more correctly the trend [Fig. 6(c), blue dashed line]. The lower drop velocities in our collective experiment, when compared to the single bursting experiment [57], could be caused by the presence of surfactants [58] or the action of neighbors around the bursting bubble [59], both effects known to disturb the jet formation process but yet to be more thoroughly understood. These might also explain the large scatter observed between different drops.

Figure 6(d) is discussed in comparison with Fig. 6(c). Below the coalescence transition $c < c_*$, bubbles merge and therefore burst at various radii [Figs. 3(a) and 3(c)], ultimately covering the size ranges of production of both jet drops and centrifuge film drops, which are measured indiscriminately. The drop ejection angle θ, shown in Fig. 6(d), offers additional information on the drop trajectories and origins. An important fraction of the drops are ejected with $\theta > 10^\circ$, and it is not uncommon to observe angles larger than 30°, as was reported for film drops from single bubbles bursting [see Fig. 2(a)]. These drops are on average larger and slower than the jet drops observed for $c \geqslant c_*$. However, for a given radius r they are ejected with a faster vertical velocity w_0, leading to

a decrease in the velocity-size relationship steeper than the scaling (1). A potential, and additional, cause for this deviation is the permanent agitation of the bubbles at the surface, not considered in the initially static modeling of jet drops. Figure 7 eventually shows the drop nondimensional velocity w_0/V_μ (i.e., the drop capillary number, Ca) as a function of its radius r/ℓ_μ (i.e., the drop Laplace number, La), from bubbles collectively bursting above the coalescence transition $c \geqslant c_*$ (pluses), compared with jet drops from bubbles bursting individually in different liquids (mixtures of glycerol, water, and ethanol, in plain dots, from Ref. [57]). As already noticed in Fig. 6, drops from bubbles collectively bursting are ejected, for a given size, at a velocity smaller than a jet drop from a single bubble (blue pluses and dots, in water). However and overall, the data from collective bursting still compare relatively well with the different liquids, with a more pronounced scatter attributed to the agitation of the bubbles at the surface. The alignment of the scaling (1) with the new set of parameters ($\alpha_J = 10.9$, $\delta_J = 26.8 \times 10^3$, thick solid black line, $\mathrm{Mo} = (\ell_\mu/\ell_c)^2 = 2.6 \times 10^{-11}$, water) and the jet drops from single bursting bubbles (green dashed line and dots, $\mathrm{Mo} = 6 \times 10^{-10}$) is incidental.

V. CONCLUSION

We report direct dynamical observations of drops produced by air bubbles bursting at the surface of water, under different levels of contamination by surfactant SDS. By acting on the stability and coalescence ability of the surface bubbles, surfactants are a practical way to tune collective effects and modify surface bubble size distributions, starting from a quasimonodisperse subsurface bubble injection. As a consequence, they select different drop production mechanisms, depending primarily on individual surface bubble sizes: jet drops when the millimetric bubbles do not merge, or a combination of jet and centrifuge film drops below the coalescence transition, when bubbles can merge. Overall, much fewer film drops are observed than jet drops, in the range of radii $r > 30\ \mu$m we resolve, confirming the statistical observation in Ref. [15]. The drop trajectories and size-velocity relationships, used to identify their production mechanism, compare well with the scaling (1) in the case of jet drops. However, in collective bursting configurations, drops of a given size appear to be ejected at a velocity slightly smaller than jet drops from a single bubble, and with a more pronounced scatter, possibly modifying the fitted coefficients in existing scalings. Collective effects, such as cascading bursting events or puncturing of nearby bubbles by horizontal centrifuge film drops, were rarely observed and are believed to affect only marginally the single bursting behavior (in avalanches of bursting events, the bursting itself is much faster than successive bursting [60]; horizontal centrifuge film drops come from nearly isolated surface bubbles and fall back into the water rapidly). The agitation of the bubbles at the surface, a direct action of surfactants, or bubble interactions are identified as possible additional causes for the large scatter around this main trend, and will require further attention in the future.

A last emphasis should be made on sizes: aerosols smaller than 10 μm lie in the lower range of usual photographic techniques, which as a consequence miss most of them. The drop trajectory analysis, an aerodynamic measurement of the drop radius, is seen as a complementary tool to bridge the gap between drop and aerosol sizes and explore smaller sizes while remaining in the visible domain. The Stokes number combines drop velocity and size and characterizes in one nondimensional number the drop likeliness to remain suspended as an aerosol particle. Even though it is here defined with respect to a gravity timescale, it can be extended to situations with a turbulent flow in the air, as would happen in more realistic oceanic conditions.

ACKNOWLEDGMENTS

This work has been supported by National Science Foundation (NSF) Grant No. 1849762, and the Cooperative Institute for Earth System modeling between Princeton and the Geophysical Fluid Dynamics Laboratory (GFDL), NOAA.

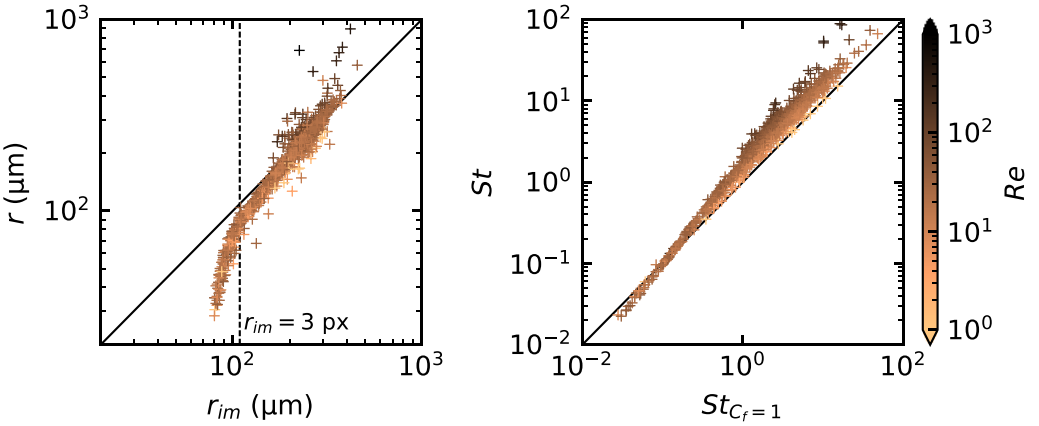

FIG. 8. (a) Drop radius, by two independent methods: r_{im} is measured by image processing, and $r = 3\sqrt{\eta_a V \mathrm{St}/2\rho g}$ is computed from the measurement of St and $V = \dot{z}(0)$ for the corresponding trajectory $z(t)$. (b) Stokes number St from the fit of Eq. (7) on experimental trajectories, using C_f from expression (A2) [56], as a function of $\mathrm{St}_{C_f=1}$ (i.e., a purely viscous drag).

APPENDIX: DRAG FORCE

From the analytical drop trajectory $z(t)$ [Eq. (7)], we immediately compute the drop fallout time t_∞ and maximal height $z_{\max}$ [also plotted on Fig. 4(b)]:

$$t_\infty = \frac{w_0}{g}\left[1 + \mathrm{St}\left(1 + W\left(-\frac{1+\mathrm{St}^{-1}}{e^{1+\mathrm{St}^{-1}}}\right)\right)\right], \quad z_{\max} = \frac{w_0^2}{g}\mathrm{St}(1 - \mathrm{St}\log(1+\mathrm{St}^{-1})), \tag{A1}$$

where W is the Lambert W function.

The fit of Eq. (7) on experimental trajectories gives access to the Stokes number and drop ejection velocity $w_0 = \dot{z}(0)$, from which we calculate the drop radius $r = 3\sqrt{\eta_a w_0 \mathrm{St}/2\rho g}$. This measure is especially valuable for drops at most a few pixels in diameter, where the accuracy of automated detection methods drops. We compare this "trajectory" radius r to the radius independently measured from image analysis r_{im} in Fig. 8(a). The agreement is good for drop radii larger than 3 pixels, as indicated by the vertical dashed line. For drop radii smaller than 3 pixels, the image radius r_{im} proves to be overestimated, and the alternate use of r over r_{im} allows us to extend the camera resolution to subpixel sizes.

Technically, we use for the drag correction factor C_f the more accurate expression by Ref. [56] (reprinted in Ref. [10]), which is applicable to Reynolds up to $\mathrm{Re} \sim \mathcal{O}(10^5)$:

$$C_f = 1 + 0.15\mathrm{Re}_t^{0.687} + \frac{0.0175\mathrm{Re}_t}{1 + 4.25\times 10^4 \mathrm{Re}_t^{-1.16}}, \quad \text{with } \mathrm{Re}_t = \mathrm{Re}|\tilde{w}(\tilde{t})|. \tag{A2}$$

This new Eq. (6) is solved numerically and fitted on the experimental trajectories so as to minimize the sum of residuals, initialized with the values from a fit on the same equation with $C_f = 1$. Figure 8 shows the correct Stokes number St as a function of the initial $\mathrm{St}_{C_f=1}$, to confirm that $\mathrm{St}_{C_f=1}$ underestimates, by a small amount, the actual drop Stokes number.

[1] A. H. Woodcock, C. F. Kientzler, A. B. Arons, and D. C. Blanchard, Giant condensation nuclei from bursting bubbles, Nature (London) **172**, 1144 (1953).

[2] D. C. Blanchard, The electrification of the atmosphere by particles from bubbles in the sea, Prog. Oceanogr. **1**, 73 (1963).

[3] J. Aitken, On dust, fogs, and clouds, Trans. R. Soc. Edinburgh **30**, 337 (1881).
[4] J. A. Day, Production of droplets and salt nuclei by the bursting of air-bubble films, Q. J. R. Meteorol. Soc. **90**, 72 (1964).
[5] J. Wu, Evidence of sea spray produced by bursting bubbles, Science **212**, 324 (1981).
[6] C. A. Tyree, V. M. Hellion, O. A. Alexandrova, and J. O. Allen, Foam droplets generated from natural and artificial seawaters, J. Geophys. Res. Atmos. **112**, D12204 (2007).
[7] R. L. Modini, L. M. Russell, G. B. Deane, and M. D. Stokes, Effect of soluble surfactant on bubble persistence and bubble-produced aerosol particles, J. Geophys. Res. Atmos. **118**, 1388 (2013).
[8] X. Wang, G. B. Deane, K. A. Moore, O. S. Ryder, M. D. Stokes, C. M. Beall, D. B. Collins, M. V. Santander, S. M. Burrows, C. M. Sultana, and K. A. Prather, The role of jet and film drops in controlling the mixing state of submicron sea spray aerosol particles, Proc. Natl. Acad. Sci. USA **114**, 6978 (2017).
[9] E. R. Lewis and S. E. Schwartz, *Sea Salt Aerosol Production: Mechanisms, Methods, Measurements and Models—A Critical Review*, Geophysical Monograph No. 152 (American Geophysical Union, Washington, DC, 2004)
[10] F. Veron, Ocean spray, Annu. Rev. Fluid Mech. **47**, 507 (2015).
[11] L. Deike, Mass transfer at the ocean-atmosphere interface: The role of wave breaking, droplets, and bubbles, Annu. Rev. Fluid Mech. **54**, 191 (2022).
[12] K. Sellegri, C. D. O'Dowd, Y. J. Yoon, S. G. Jennings, and G. de Leeuw, Surfactants and submicron sea spray generation, J. Geophys. Res. Atmos. **111**, D22215 (2006).
[13] W. C. Keene, H. Maring, J. R. Maben, D. J. Kieber, A. A. P. Pszenny, E. E. Dahl, M. A. Izaguirre, A. J. Davis, M. S. Long, X. Zhou, L. Smoydzin, and R. Sander, Chemical and physical characteristics of nascent aerosols produced by bursting bubbles at a model air-sea interface, J. Geophys. Res. Atmos. **112**, (2007).
[14] B. Néel and L. Deike, Collective bursting of free-surface bubbles, and the role of surface contamination, J. Fluid Mech. **917**, A46 (2021).
[15] B. Néel, M. A. Erinin, and L. Deike, Role of contamination in optimal droplet production by collective bubble bursting, Geophys. Res. Lett. **49**, e2021GL096740 (2022).
[16] A. A. Frossard, M. S. Long, W. C. Keene, P. Duplessis, J. D. Kinsey, J. R. Maben, D. J. Kieber, R. Y.-W. Chang, S. R. Beaupré, R. C. Cohen, X. Lu, J. Bisgrove, and Y. Zhu, Marine aerosol production via detrainment of bubble plumes generated in natural seawater with a forced-air venturi, J. Geophys. Res. Atmos. **124**, 10931 (2019).
[17] E. Fuentes, H. Coe, D. Green, G. de Leeuw, and G. McFiggans, Laboratory-generated primary marine aerosol via bubble-bursting and atomization, Atmos. Meas. Tech. **3**, 141 (2010).
[18] M. D. Stokes, G. B. Deane, K. Prather, T. H. Bertram, M. J. Ruppel, O. S. Ryder, J. M. Brady, and D. Zhao, A marine aerosol reference tank system as a breaking wave analogue for the production of foam and sea-spray aerosols, Atmos. Meas. Tech. **6**, 1085 (2013).
[19] K. A. Prather, T. H. Bertram, V. H. Grassian, G. B. Deane, M. D. Stokes, P. J. DeMott, L. I. Aluwihare, B. P. Palenik, F. Azam, J. H. Seinfeld, R. C. Moffet, M. J. Molina, C. D. Cappa, F. M. Geiger, G. C. Roberts, L. M. Russell, A. P. Ault, J. Baltrusaitis, D. B. Collins, C. E. Corrigan *et al.*, Bringing the ocean into the laboratory to probe the chemical complexity of sea spray aerosol, Proc. Natl. Acad. Sci. USA **110**, 7550 (2013).
[20] G. B. Deane and M. D. Stokes, Scale dependence of bubble creation mechanisms in breaking waves, Nature (London) **418**, 839 (2002).
[21] R. J. Cipriano and D. C. Blanchard, Bubble and aerosol spectra produced by a laboratory "breaking wave", J. Geophys. Res. **86**, 8085 (1981).
[22] D. K. Woolf, P. A. Bowyer, and E. C. Monahan, Discriminating between the film drops and jet drops produced by a simulated whitecap, J. Geophys. Res. **92**, 5142 (1987).
[23] S. F. Jones, G. M. Evans, and K. P. Galvin, Bubble nucleation from gas cavities—a review, Adv. Colloid Interface Sci. **80**, 27 (1999).
[24] H. P. Johnson, U. K. Miller, M. S. Salmi, and E. A. Solomon, Analysis of bubble plume distributions to evaluate methane hydrate decomposition on the continental slope, Geochem. Geophys. Geosyst. **16**, 3825 (2015).

[25] F. Resch, J. S. Darrozes, and G. Afeti, Marine liquid aerosol production from bursting of air bubbles, J. Geophys. Res. **91**, 1019 (1986).
[26] D. C. Blanchard and L. D. Syzdek, Film drop production as a function of bubble size, J. Geophys. Res. **93**, 3649 (1988).
[27] E. L. Andreas, J. B. Edson, E. C. Monahan, M. P. Rouault, and S. D. Smith, The spray contribution to net evaporation from the sea: A review of recent progress, Boundary Layer Meteorol. **72**, 3 (1995).
[28] A. Berny, S. Popinet, T. Séon, and L. Deike, Statistics of jet drop production, Geophys. Res. Lett. **48**, e2021GL092919 (2021).
[29] H. Lhuissier and E. Villermaux, Bursting bubble aerosols, J. Fluid Mech. **696**, 5 (2012).
[30] J. A. Day and J. C. Lease, Cloud nuclei generated by bursting air bubbles at air-sea interface, in *Proceedings of the International Conference on Cloud Physics, August 26–30, 1968, Toronto, Canada* (American Meteorological Society, Boston, MA, 1969), pp. 20–24.
[31] M. P. Paterson and K. T. Spillane, Surface films and the production of sea-salt aerosol, Q. J. R. Meteorol. Soc. **95**, 526 (1969).
[32] X. Jiang, L. Rotily, E. Villermaux, and X. Wang, Submicron drops from flapping bursting bubbles, Proc. Natl. Acad. Sci. USA **119**, e2112924119 (2022).
[33] A. Berny, L. Deike, T. Séon, and S. Popinet, Role of all jet drops in mass transfer from bursting bubbles, Phys. Rev. Fluids **5**, 033605 (2020).
[34] L. Deike, É. Ghabache, G. Liger-Belair, A. K. Das, S. Zaleski, S. Popinet, and T. Séon, Dynamics of jets produced by bursting bubbles, Phys. Rev. Fluids **3**, 013603 (2018).
[35] A. M. Gañán-Calvo, Revision of Bubble Bursting: Universal Scaling Laws of Top Jet Drop Size and Speed, Phys. Rev. Lett. **119**, 204502 (2017).
[36] É. Ghabache, G. Liger-Belair, A. Antkowiak, and T. Séon, Evaporation of droplets in a Champagne wine aerosol, Sci. Rep. **6**, 25148 (2016).
[37] C. F. Brasz, C. T. Bartlett, P. L. L. Walls, E. G. Flynn, Y. E. Yu, and J. C. Bird, Minimum size for the top jet drop from a bursting bubble, Phys. Rev. Fluids **3**, 074001 (2018).
[38] A. M. Gañán-Calvo, Scaling laws of top jet drop size and speed from bubble bursting including gravity and inviscid limit, Phys. Rev. Fluids **3**, 091601 (2018).
[39] A. M. Gañán-Calvo and J. M. López-Herrera, On the physics of transient ejection from bubble bursting, J. Fluid Mech. **929**, A12 (2021).
[40] J. M. Gordillo and J. Rodríguez-Rodríguez, Capillary waves control the ejection of bubble bursting jets, J. Fluid Mech. **867**, 556 (2019).
[41] F. J. Blanco-Rodríguez and J. M. Gordillo, On the sea spray aerosol originated from bubble bursting jets, J. Fluid Mech. **886**, R2 (2020).
[42] D. E. Spiel, A hypothesis concerning the peak in film drop production as a function of bubble size, J. Geophys. Res. **102**, 1153 (1997).
[43] D. E. Spiel, On the births of film drops from bubbles bursting on seawater surfaces, J. Geophys. Res. **103**, 24907 (1998).
[44] F. Resch and G. Afeti, Submicron film drop production by bubbles in seawater, J. Geophys. Res. **97**, 3679 (1992).
[45] S. Poulain, E. Villermaux, and L. Bourouiba, Ageing and burst of surface bubbles, J. Fluid Mech. **851**, 636 (2018).
[46] H. B. Squire, Investigation of the instability of a moving liquid film, Br. J. Appl. Phys. **4**, 167 (1953).
[47] G. M. Afeti and F. J. Resch, Distribution of the liquid aerosol produced from bursting bubbles in sea and distilled water, Tellus B: Chem. Phys. Meteorol. **42**, 378 (1990).
[48] D. Shaw and L. Deike, Film drop production over a wide range of liquid conditions (unpublished).
[49] Y. Toba, Drop production by bursting of air bubbles on the sea surface (II) theoretical study on the shape of floating bubbles, J. Oceanogr. Soc. Jpn. **15**, 121 (1959).
[50] G.-S. Yeom, Correlations and asymptotic behaviors of the shape parameters of floating bubbles using an improved numerical procedure, Appl. Sci. **12**, 1804 (2022).
[51] Y. M. Yang and J. R. Maa, Bubble coalescence in dilute surfactant solutions, J. Colloid Interface Sci. **98**, 120 (1984).

[52] T. O. Oolman and H. W. Blanch, Bubble coalescence in stagnant liquids, Chem. Eng. Commun. **43**, 237 (1986).
[53] L. Schiller and A. Naumann, A drag coefficient correlation, Z. Ver. Deutsch. Ing. **77**, 318 (1933).
[54] M. P. Rouault, P. G. Mestayer, and R. Schiestel, A model of evaporating spray droplet dispersion, J. Geophys. Res.: Oceans **96**, 7181 (1991).
[55] D. E. Spiel, The number and size of jet drops produced by air bubbles bursting on a fresh water surface, J. Geophys. Res. **99**, 10289 (1994).
[56] R. Clift and H. W. Gauvin, The motion of particles in turbulent gas streams, in *Chemical Engineering Conference Australia 1970: Melbourne and Sydney (Chemeca '70)* (Butterworths, London, 1970), pp. 14–28.
[57] É. Ghabache, Surface libre hors équilibre: De l'effondrement de cavité aux jets étirés, Ph.D. thesis, Université Pierre et Marie Curie-Paris VI (2015).
[58] C. R. Constante-Amores, L. Kahouadji, A. Batchvarov, S. Shin, J. Chergui, D. Juric, and O. K. Matar, Dynamics of a surfactant-laden bubble bursting through an interface, J. Fluid Mech. **911**, A57 (2021).
[59] T. Séon and G. Liger-Belair, Effervescence in champagne and sparkling wines: From bubble bursting to droplet evaporation, Eur. Phys. J. Spec. Top. **226**, 117 (2017).
[60] H. Ritacco, F. Kiefer, and D. Langevin, Lifetime of Bubble Rafts: Cooperativity and Avalanches, Phys. Rev. Lett. **98**, 244501 (2007).